Compact Plasmonic Distributed-Feedback Lasers as Dark Sources of Surface Plasmon Polaritons

Journal Article

Author(s):
Brechbühler, Raphael (ID); Vonk, Sander J.W.; Aellen, Marianne; Lassaline, Nolan; Keitel, Robert (ID); Cocina, Ario; Rossinelli, Aurelio (ID); Rabouw, Freddy T.; Norris, David J. (ID)

Compact Plasmonic Distributed-Feedback Lasers as Dark Sources of Surface Plasmon Polaritons

Raphael Brechbühler,[†] Sander J. W. Vonk,[†,§] Marianne Aellen,[†] Nolan Lassaline,[†] Robert C. Keitel,[†] Ario Cocina,[†] Aurelio A. Rossinelli,[†] Freddy T. Rabouw,[†,§] and David J. Norris*,[†]

[†]Optical Materials Engineering Laboratory,
Department of Mechanical and Process Engineering,
ETH Zurich, 8092 Zurich, Switzerland

[§]Debye Institute for Nanomaterials Science,
Utrecht University, 3584 CC Utrecht, The Netherlands

ABSTRACT. Plasmonic modes in optical cavities can be amplified through stimulated emission. Using this effect, plasmonic lasers can potentially provide chip-integrated sources of coherent surface plasmon polaritons (SPPs). However, while plasmonic lasers have been experimentally demonstrated, they have not generated propagating plasmons as their primary output signal. Instead, plasmonic lasers typically involve significant emission of free-space photons that are intentionally outcoupled from the cavity by Bragg diffraction or that leak from reflector edges due to uncontrolled scattering. Here, we report a simple cavity design that allows for straightforward extraction of the lasing mode as SPPs while minimizing photon leakage. We achieve plasmonic lasing in 10-µm-long distributed-feedback cavities consisting of a Ag surface periodically patterned with ridges coated by a thin layer of colloidal semiconductor nanoplatelets as the gain material. The diffraction to free-space photons from cavities designed with second-order feedback allows a direct experimental examination of the lasing-mode profile in real- and momentum-space, in good agreement with coupled-wave theory. In contrast, we demonstrate that first-order-feedback cavities remain "dark" above the lasing threshold and the output signal leaves the cavity as propagating SPPs, highlighting the potential of such lasers as on-chip sources of plasmons.

Surface plasmon polaritons (SPPs) are electromagnetic surface waves bound to a metal–dielectric interface.[1,2] Various surface structures have been studied to concentrate plasmons to trenches, slots, and wedges, creating hot spots of strongly enhanced near-field intensities.[3] By boosting light–matter interactions, such hot spots enable the detection of weak signals for optical sensing,[4] strengthen non-linear effects,[5–7] and allow the design of miniaturized optical devices such as plasmonic switches[8] and modulators[9] with low driving voltage and high speed. In many state-of-the-art plasmonic circuits, SPPs are generated by coupling photons from an external laser source directly to a plasmonic mode *via* a plasmonic grating coupler[9] or a two-step process involving a photonic grating coupler followed by a photon–plasmon converter.[10] This incoupling requires external optical components with precise alignment, increasing the size and complexity of the final device. Alternatively, chip-integrated photonic microlasers with subsequent conversion of the output to a plasmonic mode have been demonstrated, although with limited conversion efficiency.[11,12]

Instead of using these photon-to-plasmon conversion processes, plasmonic devices could utilize direct on-chip sources of intense and coherent SPPs. This approach could then lead to integrated optical devices with reduced footprint and complexity. Plasmonic lasers could provide such a source, as they can locally generate coherent plasmons.[13–15] Namely, a gain material amplifies a plasmonic mode in a cavity by means of stimulated emission. Once the gain exceeds the losses of the cavity mode, plasmonic lasing results.[16] While devices based on localized surface plasmon resonances (LSPRs), as proposed by Bergman and Stockman,[14] could result in truly nanoscopic lasers (often called spasers), efficient coupling of the output to an extended plasmonic circuit would be challenging. On the other hand, lasers based on SPP modes[13] could directly serve as SPP sources for miniaturized plasmonic chips.

To explore such SPP-based plasmonic lasers, plasmonic cavities defined by bulk metallic reflectors,[17–19] grating-based reflectors,[20] and terminated waveguides[15,21–24] have been prepared. Despite the variety of reflector designs, extracting the output signal from such cavities as a guided SPP mode propagating in a well-defined direction remains a major hurdle for creating on-chip SPP sources. Cavity reflectors also typically introduce sharp discontinuities that can lead to scattering of

the plasmonic signal to unwanted modes (such as free-space photons), limiting the efficiency and complicating a quantitative analysis of the SPP output.[24]

These problems can be mitigated by distributing the feedback over the entire cavity length. In plasmonic distributed-feedback (DFB) lasers, counter-propagating SPPs on a metal–dielectric interface are coupled by diffraction at periodically arranged subwavelength scatterers. Recent experimental demonstrations[25–29] highlight that DFB cavities offer a suitable platform for plasmonic lasing in the visible and near-infrared spectral range. So far, such plasmonic DFB cavities have been designed predominantly with second-order feedback to diffract the lasing output to free-space photons, which is not ideal for SPP sources.[25–28] While designs that avoid photon leakage by utilizing first-order-feedback cavities are widely employed in edge-emitting photonic DFB lasers, they remain largely unexplored in plasmonic systems.[29] In particular, a plasmonic distributed-feedback laser that outputs the entire lasing signal as tightly confined SPPs propagating on a metal–dielectric interface has not yet been demonstrated.

Here, we present a plasmonic distributed-feedback laser that allows for straightforward extraction of the lasing signal as propagating SPPs without diffractive photon leakage. Our design consists of an optically thick Ag surface patterned with periodic ridges (*i.e.* a grating) to form the DFB cavity (10 μm in length). We then place colloidal CdSe nanoplatelets with graded $Cd_xZn_{1-x}S$ shells on this structure to provide gain. Plasmonic lasing is observed at visible wavelengths upon optical excitation of the gain material. To maximize the distributed-feedback strength of our cavities, we optimized the ridge geometry based on spatial-frequency considerations ("Fourier design").[30] The anticipated trends were verified by experimentally extracting the stop-gap widths of our cavities as a function of the ridge dimensions. We first study second-order-feedback cavities, which use the second spatial harmonic (second Fourier component) of the grating for plasmonic feedback. The fundamental spatial frequency couples a fraction of the plasmonic lasing signal to free-space photons through Bragg diffraction. Although such photon diffraction is a loss pathway for SPP sources that increases the lasing threshold and reduces the extraction efficiency of SPPs, it allows examination of the far-field lasing-mode profiles both in real- and *k*-space. After establishing the operation of this second-order-feedback

design, we proceed to cavities with first-order feedback, which exploit the fundamental spatial frequency of the grating. In such devices, Bragg diffraction of the plasmonic signal to free-space photons is prohibited. Consequently, above the lasing threshold, these DFB cavities remain "dark" in the far field. This allows the lasing mode to leave the cavity as propagating SPPs, which we study by placing outscatterers at a distance from the cavity. Our findings highlight the potential of plasmonic DFB lasers as miniaturized on-chip sources of SPPs and provide simple guidelines for engineering the feedback strength as well as experimental methods for probing the plasmonic output.

RESULTS AND DISCUSSION

Plasmonic Distributed-Feedback Cavities. We begin by discussing plasmonic DFB cavities without a gain material. We fabricated optically thick plasmonic surfaces patterned with periodic ridges by depositing Ag on prepatterned Si substrates, followed by template stripping (see Methods and Section S1 in the Supporting Information for details).[31] The scanning-electron micrograph in Figure 1a shows the edge of a Ag grating with a pitch (p) of 560 nm and a duty cycle (d) of 2/3, where the duty cycle is defined as the fraction of the pitch occupied by the ridge ($d = r / p$ in Figure 1a). Various pitches p and duty cycles d were realized by adapting the pattern on the same Si template. Various ridge heights h were achieved by varying the etching depth on different Si templates. These depths were then measured by profilometry ($h = 13$ nm in Figure 1a).

To study the SPP modes on a Ag surface covered with a thin dielectric layer, we coated our plasmonic gratings with a ~50-nm-thick film of poly(methyl methacrylate), PMMA. This Ag–dielectric–air stack supports surface plasmon polaritons with transverse-magnetic (TM) polarization. The real part of their in-plane wavevector, $\boldsymbol{k}_{\mathrm{SPP}}$, has a magnitude of $k_{\mathrm{SPP}} = k_0 \, n_{\mathrm{SPP}}(\omega)$, where $k_0 = \omega/c$ is the wavevector of free-space photons, ω the angular frequency, c the speed of light, and $n_{\mathrm{SPP}}(\omega)$ the real part of the frequency-dependent effective mode index of the SPP mode. We calculated $n_{\mathrm{SPP}}(\omega)$ for a flat three-layer geometry (neglecting the ridges) by solving Maxwell's equations with boundary conditions at the interfaces.[32] Figure 1b plots the real part of the in-plane wavevector of SPPs as red lines (see Section S2 in the Supporting Information). A plasmonic grating periodic in one dimension (1D) along x (Figure 1a) couples SPPs to modes with in-plane wavevector

$$\boldsymbol{k}_{||} = \boldsymbol{k}_{\text{SPP}} + \boldsymbol{g}_n \tag{1}$$

where $\boldsymbol{g_n} = ng\hat{\boldsymbol{x}}$ is the grating momentum vector with $n = \pm1, \pm2, \pm3$, *etc.*, $\hat{\boldsymbol{x}}$ is the unit vector along x, and $g = 2\pi/p$ is the magnitude of the reciprocal lattice vector of the grating. SPPs can couple to free-space photons (below referred to as SPP−photon coupling or, by reciprocity, photon−SPP coupling) if $|\boldsymbol{k}_{||}|$ in eq 1 is smaller than k_0 (solid black diagonal lines, or "light lines," in Figure 1b).

Making use of photon–SPP coupling, we experimentally probe the dispersion relation using a Fourier-imaging setup[33,34] (see Methods and Section S3 in the Supporting Information). Figure 1b shows the measured momentum-resolved reflectivity spectrum as a colormap for the grating in Figure 1a. (Experimental data for gratings with other parameters are provided in Figure S1 in the Supporting Information.) The blue areas in the colormap represent coupling of incoming light with in-plane wavevector $\boldsymbol{k}_{||} = k_x\hat{\boldsymbol{x}}$ to SPPs through interaction with the grating (see horizontal black arrows). This coupling decreases the intensity of the reflected signal. The dispersion of these reflectivity dips deviates from the simple predictions of eq 1 (black dashed lines) around ~1.9 and ~2.8 eV (and in Figure S1 in the Supporting Information at ~2.5 eV). At these energies we experimentally observe avoided crossings and the formation of stop gaps. These stop gaps originate from coupling of SPPs propagating in the +x and −x directions *via* grating momentum g_n,[35] occurring when

$$2k_{\text{SPP}} = g_n \tag{2}$$

(below referred to as the g_n-feedback condition; indicated for g_2 in Figure 1b with a red horizontal double arrow). While no SPPs can propagate in ±x on the grating at energies within the stop gap, SPP–SPP coupling provides distributed feedback for SPP modes at the corresponding stop-gap edges. In fact, a large coupling rate—observable in our data as an energetically wide stop gap—has been shown to lower the lasing threshold of DFB lasers.[36]

Therefore, we seek ridge geometries that maximize the SPP–SPP coupling rate for plasmonic DFB cavities. We first examine structures operating at the g_2-feedback condition (often called "second-order feedback"). This feedback rate can be calculated from the stop-gap widths (ΔE_{g_2}) measured in our reflectivity maps. Gratings with a common pitch of 560 nm and various duty cycles feature distinctively different stop gaps, as seen in Figure 1c. (For data on other grating parameters

see Figure S1 in the Supporting Information.) We extract the feedback rate at the g_2-feedback condition (Γ_{g_2}) by fitting a coupled-mode model to the reflectivity data (coupled modes shown as red dashed lines; see Section S2 in the Supporting Information).[37] The extracted rates are depicted with filled circles in Figure 1d. The feedback increases for larger ridge heights and is maximized for duty cycles of 1/4 and 3/4.

In addition to the feedback rate, the choice of duty cycle also affects the coupling of the plasmonic modes at the stop-gap edges to photons. Figure 1c and Figure S1 in the Supporting Information show that the reflectivity dip disappears at the lower-energy (higher-energy) edge for duty cycles smaller (larger) than 1/2. Thus, SPPs at the corresponding edge cannot couple to free-space photons. The occurrence of such "dark" plasmonic modes at stop-gap edges has been discussed[35] and can be attributed to destructive interference of the diffracted light in the far field.[38] Correspondingly, DFB lasers operating at the dark edge of the g_2 stop gap show a lowered lasing threshold because of reduced photon leakage.[27,38,39] However, the destructive interference can only be partial because the feedback cavity is not infinitely extended in space. Thus, the lasing modes will have a finite width in k_x, allowing photon leakage away from the stop-gap edge, which exists exactly at $k_x = 0$ μm^{-1} (Figure 1c).[27]

As mentioned above, a better strategy to eliminate cavity leakage is to operate the plasmonic DFB laser at the g_1-feedback condition ("first-order feedback"), where counter-propagating SPP modes are coupled by g_1. Outcoupling to free space *via* grating diffraction is then not allowed because the available grating momenta g_n are too large to diffract SPPs to photons ($|\pm k_{\text{SPP}} \mp g_n| > k_0$ for all n). However, while preventing SPP–photon diffraction reduces undesired losses from the plasmonic cavity, it also makes direct study of the dark cavity modes challenging. Thus, to probe the g_1 stop-gap width (ΔE_{g_1}), we utilized samples with structures as depicted in Figure 1e. SPPs are launched at a photon−SPP incoupling grating, propagate in the $+x$ direction over the feedback cavity, and the transmitted signal is collected at an SPP−photon outcoupling grating (see Methods and Section S3 in the Supporting Information). We investigated feedback cavities with a pitch of 280 nm, such that the g_1 stop gap occurred at the same energy (~1.9 eV) as the g_2 stop gap in Figures 1a–d (see eq 2). SPPs at energies within the stop gap cannot propagate across the feedback cavity along $\hat{x}$, resulting in a dip

in the SPP-transmission spectra (Figure 1f) centered around the energy estimated using eq 2 (dashed black line). From the width of the stop gaps we calculated the coupling rates at the g_1-feedback condition Γ_{g_1} (filled circles in Figure 1g), which shows that the strongest g_1 feedback is realized for duty cycles around ~1/2. This is clearly different from g_2 feedback, which shows a minimum for this duty cycle (Figure 1d).

The observed trends in Figure 1d,g can be understood through Fourier decomposition of the height profiles $H(x)$ of our gratings into spatial-frequency components:

$$H(x) \ = \ \sum_{n=1,2,3,\dots} a_n \cos(g_n x) \tag{3}$$

where $a_n(d,h) = 2h \sin(n\pi d)/(n\pi)$ are the Fourier coefficients, which depend on the duty cycle.[40] The first (second) Fourier component, with coefficient a_1 (a_2), dominates diffraction by g_1 (g_2) in the limit of shallow gratings, *i.e.*, $h/\lambda \ll 1$.[30,35,39] Indeed, we find a linear relationship (Figure S2 in the Supporting Information) when the experimentally obtained coupling rates $\Gamma_{g_n}(d,h)$ are plotted against $|a_n(d,h)|$ for $n = 1$ and 2. The fitted slope is then used as a single, global parameter to reproduce the experimental data in Figure 1d,g (solid lines). Thus, the functional form of $a_n(d,h)$ provides simple guidelines to maximize the feedback rate for plasmonic DFB lasers.

Design of Plasmonic Lasers. We now include a gain material in our DFB cavities. Based on the discussion above, we consider two types of lasers: (i) "leaky" plasmonic DFB lasers operating with g_2 feedback near the stop-gap edge and (ii) "dark" plasmonic DFB lasers operating with g_1 feedback. For each case, we employed the appropriate duty cycle (Figure 1d,g) to maximize the distributed feedback (see Methods for details). To analyze the output, we placed outscattering gratings 2.5 μm from the 10×10-μm^2-sized feedback cavity (Figure 2a) such that they interact with SPPs that leave the feedback cavity in the $\pm x$ directions. These outscattering gratings were designed to minimize SPP reflection while maximizing diffraction into photons with an outgoing direction close to the surface normal. Next, we deposited a thin layer of colloidal nanoplatelets (NPLs) with 4-monolayer-thick CdSe cores and graded Cd$_x$Zn$_{1-x}$S shells[41] onto the Ag surface by drop-casting from a liquid dispersion (see Methods). CdSe-based NPLs exhibit high material gain in the visible spectral range[42] and have been successfully integrated into lasing devices.[19,43] The addition of graded shells to the NPLs increases

their photoluminescence quantum yield and photostability.[41] The NPLs arrange into ~50-nm-thick densely packed films that uniformly coat the gratings, as seen in the scanning-electron micrograph in Figure 2b. At this NPL-layer thickness, only the plasmonic mode (*i.e.* the lowest-order TM mode) can exist, while higher-order TM modes and all TE modes are cut off.[19] For our lasing experiments, we cooled the samples to 4 K in a cryostat and we optically excited the NPLs with a pulsed laser source (pulse length ~340 fs) at 2.583 eV (480 nm) with a repetition rate of 100 Hz. The excitation laser spot was prepared with a flat-top spatial profile to obtain spatially uniform excitation of the NPLs (see Section S3 in the Supporting Information).

Plasmonic Lasing with Leaky DFB Cavities. We start our lasing experiments with a "leaky" DFB cavity operating with g_2 feedback [feedback cavity (outscattering gratings) with $p = 435$ nm, $h = 11$ nm, and duty cycle d of 3/4 (1/2)]. First, we optically excited only the NPLs on the feedback cavity without exciting the surrounding area (see Methods). Figure 2c shows a momentum-resolved emission spectrum at an excitation fluence of 23 μJ cm^{-2} (see Methods). We attribute the broad feature centered at ~1.94 eV to direct spontaneous emission of photons from the NPLs emitted into all angles (all k_x values) within the numerical aperture (NA of 0.7) of our collection objective. Additional weak features can be observed in Figure 2c close to $k_x = 0$ μm^{-1} due to spontaneous emission of SPPs through near-field coupling of the NPLs, followed by diffraction to photons by the feedback cavity. These collected photons probe the grating dispersion with the reverse process as in our reflectivity measurements above (SPP−photon coupling instead of photon−SPP coupling). From the energies of the two g_2 stop-gap edges (seen as faint features indicated with white arrows in Figure 2c) and the stop-gap center energy, we estimate a feedback rate of 50 ps^{-1} and an effective mode index n_{SPP} of 1.48, respectively. At excitation fluences above ~25 μJ cm^{-2} (comparable to values for which we have previously observed plasmonic lasing in plasmonic Fabry–Pérot cavities with the same gain material[19]) two bright spots appear in the momentum-resolved emission spectrum at the higher-energy stop-gap edge (Figure 2d at an excitation fluence of 52 μJ cm^{-2}). We attribute the two spots to plasmonic distributed-feedback lasing close to the "dark" stop-gap edge (*cf.* right-most panel of Figure 1c). The lasing feature has a full-width at half-maximum of ~4 meV as seen after integration over all

k_x (red line in Figure 2e; the resolution of the optical system is ~0.7 meV). Preliminary experiments suggest that the linewidth measured for our devices is narrower for individual lasing pulses and shows broadening due to slight spectral fluctuations from pulse to pulse (here, integrated over 50 laser pulses). We note that plasmonic lasing was also observed at higher cryogenic temperatures (30, 80, 130, and 180 K) but not when we subsequently warmed up to room temperature.

Next, we investigated the real-space profile of the lasing mode and the fraction of lasing emission that leaves the grating as SPPs bound to the Ag surface. To minimize reabsorption of SPPs by unpumped NPLs between the feedback cavity and the outscattering gratings, we increased the size of our flat-top excitation spot to cover the feedback cavity, the outscattering gratings, and the area in between. Real-space images of the lasing emission in a ~5-meV spectral range centered around the lasing energy are collected by using a tunable bandpass filter in our collection path (see Methods). Below the threshold fluence, we observed spontaneous emission from the entire excited area (Figure 3a at 19 μJ cm^{-2}). Above the lasing threshold, the feedback cavity (indicated with a white square box) as well as the neighboring regions on the outscatterers (white rectangular boxes) appear significantly brighter than the rest of the pumped area (Figure 3b at 39 μJ cm^{-2}). The signal detected on the feedback cavity stems from leakage of the plasmonic lasing signal to photons *via* diffraction by g_1 and is a loss channel (green arrow in Figure 3c). The bright areas on the outscatterers correspond to the desired output channel: SPPs leave the cavity in the $\pm x$ directions (feedback direction) and are subsequently diffracted by the outscatterers (blue arrows in Figure 3c). Figure 3d depicts line traces through the above-threshold real-space image (Figure 3b) averaged over the width of the feedback cavity (black line; $|y| < 5$ μm) and over the areas just below and above (red line; 5 μm $< |y| < 10$ μm). The green shaded area corresponds approximately to the far-field lasing-mode profile on the feedback cavity after subtraction of the background spontaneous emission. This area represents ~40% of the total collected lasing output (sum of green and blue shaded areas). The lasing-mode profile features a minimum in the center ($x = 0$ μm) and increases towards both ends of the cavity ($x \approx \pm 5$ μm).

We can understand this profile with coupled-wave theory, which was originally introduced for photonic DFB lasers[36] and recently applied to plasmonic lasers.[27,44] The theory considers counter-

propagating plane waves $R(x) \exp(-ik_{SPP}x)$ and $S(x) \exp(ik_{SPP}x)$, travelling in the $+x$ and $-x$ directions over the feedback cavity, respectively, with smoothly varying complex electric-field envelopes $R(x)$ and $S(x)$. The plane waves are subject to gain and weak scattering at a periodic perturbation (here, the ridges of the feedback cavity), leading to coupling between the waves close to the stop-gap edges. Using this coupled-wave formalism with our experimentally determined feedback rate as input, we computed $R(x)$ and $S(x)$ for the lasing mode with the lowest threshold at the "dark" stop-gap edge,[27,39] depicted in Figure 3e as the far-field intensity profile $I(x) = |R(x) + S(x)|^2$ (see Section S2 in the Supporting Information). The profile features a node at $x = 0$ µm, where the diffracted signals of $R(x)$ and $S(x)$ destructively interfere in the far field, in qualitative agreement with the experimental real-space profile of the lasing mode (black line in Figure 3d, over the green-shaded range $|x| < \sim 5$ µm). However, the spontaneous-emission background in our experimental data renders a quantitative comparison of the real-space patterns difficult.

To analyze further, we reduced the background caused by spontaneous emission and scattering from defects by imaging the lasing signal from the DFB cavity in k-space while blocking the signal from the outscatterers using a real-space aperture in the detection path (see Methods and Section S3 in the Supporting Information). Spontaneous emission and defect scattering is spread over all emission angles (k_x and k_y values) while the grating-mediated outcoupling of the lasing signal appears as two well-defined lobes centered around $k_x / k_0 = 0$ with a spread in k_y due to the finite size of the lasing mode along the y direction (Figure 3f; 40 µJ cm^{-2}). The intensity collected from the two lobes (integrated over white dashed area) is nearly absent below the lasing threshold and strongly increases once a threshold fluence of ~ 25 µJ cm^{-2} is reached (Figure 3g), indicating that the lobes indeed correspond to the lasing leakage signal. A crosscut of the angular emission distribution from Figure 3f around $k_y / k_0 = 0$ is presented as the green curve in Figure 3h. We overlay the prediction from coupled-wave theory (black line). The result was converted to k-space through $I(k_x) = I_0|\mathcal{F}[R(x) + S(x)]|^2$, where $\mathcal{F}$ represents the Fourier transform. Using the experimentally determined coupling rate and a fitted scaling constant I_0, we find very good agreement between the

theoretical prediction and the experimental output. Hence, the two-lobed patterns observed in Figures 2d and 3f indeed correspond to distributed-feedback lasing diffracted into the light cone by g_1.

Plasmonic Lasing with Dark DFB Cavities. Now that we understand plasmonic lasing with feedback by g_2, we turn to lasing at the g_1-feedback condition. The latter is experimentally more difficult to study. In principle, no photon-leakage channel exists, and the entire plasmonic signal should leave the cavity as propagating SPPs. Thus, the feedback cavity should remain completely dark above the lasing threshold. For our experiments, we chose a feedback cavity with $p = 201$ nm, $h = 11$ nm, and $d = 1/2$, optimized to maximize g_1 feedback. The outscattering gratings had the same h and d, but $p = 402$ nm to diffract the SPP output to photons. Lasing measurements were conducted with optical excitation of the feedback cavity, the outscattering gratings, and the area in between. In a momentum-resolved emission spectrum with optical excitation below the lasing threshold (Figure 4a at 13 μJ cm^{-2}), we observed spontaneous emission of photons under all angles as well as spontaneous emission of SPPs that diffracted into photons at the outscattering gratings around $k_x = 0$ μm^{-1}. At excitation fluences above ~19 μJ cm^{-2}, two spectrally narrow emission peaks at slightly different energies can be observed (Figure 4b at 40 μJ cm^{-2}), depicted in Figure 4c after integrating the momentum-resolved emission spectra over all collected k_x. The peaks are attributed to two plasmonic lasing modes at the higher-energy g_1 stop-gap edge of the cavity grating. The origin of the two modes will be discussed further below.

We again collected real-space images of the lasing signal by filtering a ~6.5-meV spectral range around the lasing energy using a tunable bandpass filter. Above the lasing threshold (Figures 4d at 40 μJ cm^{-2}; below-threshold image in Figure S3a in the Supporting Information) we observe a strong signal on the central regions of the outscatterers ($|y| < 5$ μm). In contrast to g_2-feedback lasing (Figure 3b), the g_1-feedback cavity remains dark in the far field apart from a weak signal attributed to defects on the feedback cavity (see center of Figure 4d). This is consistent with the absence of a grating component that could couple SPPs on the feedback cavity to free-space photons (see schematic in Figure 4e). The leakage by scattering at defects on the feedback cavity is estimated as the green area in Figure 4g. In comparison, the SPP output intensity detected on the outscatterers (estimated as the

blue area) is significantly larger. We estimate that ~80% of the energy in the lasing mode leaves the DFB cavity as propagating SPPs. This value is conservative because a fraction of the SPPs is transmitted through the outscattering gratings as is evident from the remaining signal at the outer edges of the outscatterers in Figure 4g. Plasmonic DFB lasers operating with g_1 feedback therefore have the potential to be employed as chip-integrated sources of SPPs with minimal losses due to diffraction to photons.

To understand the two lasing modes at slightly different energies observed in Figure 4b,c, we recorded the angular emission distribution of the lasing signal collected from the outscatterers by k-space imaging. Below threshold, we observe two weak arcs (Figure S3b in the Supporting Information), corresponding to spontaneously emitted SPPs incident on the outscattering gratings from different in-plane directions and diffracted into the light cone (eq 1). Above threshold (Figure 4f at 40 µJ cm^{-2}), a strong signal emerges on the two arcs at small k_y. (The fluence-dependent intensity of the signal is plotted in Figure S3c in the Supporting Information.) This signal stems from the lasing output that propagates as SPPs away from the feedback cavity in $\pm x$ and diffracts into photons at the outscatterers. The node in this signal at $k_y / k_0 = 0$ shows that the predominantly collected DFB lasing mode is a higher-order transverse mode with opposite phase at positive and negative y positions and a node at $y = 0$ µm. We hypothesize that the large g_1 stop-gap width of our feedback-optimized cavities (around twice as large as for the g_2 stop gap for a given h; compare Figure 1d,g) leads to significant reflection at the transverse cavity edges because of the large momentum mismatch between SPPs propagating in the cavity and on the surrounding flat Ag–NPL interface. This could result in confinement of lasing modes in the transverse direction. In line with this interpretation, we have found such transverse modes also for g_2-feedback lasing in preliminary experiments with larger ridge heights of 19 nm (instead of 11 nm in Figure 3).

CONCLUSIONS

In summary, we have demonstrated plasmonic distributed-feedback lasing with "leaky" second-order-feedback and "dark" first-order-feedback cavities. By probing the stop-gap widths of cavities as a function of the ridge geometry, we have experimentally determined the grating parameters that

maximize the cavity feedback strength and thus minimize the device threshold.[36] After combining the optimized cavities with a thin film of colloidal NPLs as a gain material we have observed plasmonic lasing in our devices upon optical pumping. The lasing mode of devices with second-order feedback was studied by collecting the cavity leakage from diffraction into the light cone. By selectively collecting emission at the lasing energy, the far-field mode profiles were studied in real- and *k*-space. Good agreement between the above-threshold mode profile and predictions from an established coupled-wave theory was demonstrated using experimentally obtained values for the feedback rate. Although this second-order lasing device is operated at the dark stop-gap edge, the finite size of the lasing mode leads to unavoidable cavity leakage. In contrast, we experimentally showed that devices with first-order feedback feature no cavity leakage except from weak scattering at local defects. We probed the lasing output, which leaves the distributed-feedback cavity as propagating SPPs, with spatially separated outscattering gratings. Our results highlight that plasmonic first-order distributed-feedback lasers are a promising platform for on-chip sources of plasmons.

METHODS

Fabrication of Templates for 1D Gratings. A four-inch Si wafer was diced into 2×2-cm^2-sized chips. Then, a layer of AR-P 6200.04 resist was spin-coated onto the chips, and grating structures with varying parameters were defined using electron-beam lithography. After developing the resist, the pattern was transferred into the Si substrates using HBr-based reactive-ion etching. Finally, the resist was removed. A complete description of the template fabrication is available in Section S1 in the Supporting Information.

Template-Stripping of Plasmonic Ag Gratings. Approximately 700 nm of Ag was evaporated onto the Si templates at a rate of 25 Å/s using a thermal evaporator at a pressure below 4×10^{-7} mbar.[45] Then, a glass slide was affixed on the exposed Ag surface with epoxy, the epoxy was cured by exposure to an ultraviolet lamp, and the Ag–epoxy–glass stack was stripped from the Si template, revealing a smooth Ag surface with the negative of the initial pattern in the Si template.[31] More information on the template-stripping process is available in Section S1 in the Supporting Information.

Spin-Coating of PMMA on Ag Surfaces. For the structures discussed in Figure 1b–d,f,g, the plasmonic surfaces were covered with a ~50-nm-thick layer of PMMA by spin-coating a solution of 2 weight percent PMMA in anisole at 3000 rpm for 1 min.

Deposition of NPL Films on Ag Surfaces. For the structures discussed in Figures 2–4, four-monolayer-thick colloidal CdSe nanoplatelets with graded shells of $Cd_xZn_{1-x}S$ were drop-casted onto the plasmonic surfaces without PMMA. A detailed description of the synthesis procedure and a characterization of the NPLs is given in Ref. 41 (labeled as "4-ML-CdSe/$Cd_xZn_{1-x}S$"). The stock dispersion was stored in hexane at an optical density of 9 at the lowest-energy excitonic peak measured over an optical path length of 1 cm. 5 parts of the stock dispersion were diluted with 5 parts of hexane and 1 part of octane by volume, and 40 μL of the diluted NPL dispersion were drop-casted onto a ~2.2×2.2-cm²-sized substrate. More details on the NPL-deposition process is provided in Section S1 in the Supporting Information.

Reflectivity Measurements. To measure momentum-resolved reflectivity spectra, a sample containing plasmonic gratings covered with a thin layer of PMMA was mounted on an inverted microscope in the focus of a microscope objective (NA of 0.8). The sample was excited with a broadband halogen lamp from all angles by imaging the filament of the lamp onto the back focal plane of the objective after reflection off a beam-splitter (see schematic of the optical setup in Figure S4a in the Supporting Information). The light reflected off the sample was collected through the same microscope objective, and, after transmission through the beam splitter, the Fourier image of the reflected signal was projected onto a 50-μm-wide entrance slit of an imaging spectrograph. A linear polarizer was placed in the collection path to selectively transmit light with electric fields along the entrance slit. The signal transmitted through the slit was a slice through k-space near $k_y / k_0 = 0$. We spectrally dispersed this signal with the imaging spectrograph and recorded the resulting image using a complementary metal-oxide-semiconductor (CMOS) camera. Each momentum-resolved spectrum was normalized by a similarly obtained reference spectrum reflected off a flat Ag surface covered with the same PMMA film. A detailed description of the optical setup is available in Section S3 of the Supporting Information. Each studied grating had a width in the y direction of 50 μm and a length in

the x direction (feedback direction) given by the maximum integer multiple of the pitch that yielded a length below 50 μm.

SPP-Transmission Measurements. To probe the g_1 stop gap of our plasmonic DFB cavities, SPPs were launched by an incoupling grating, propagated along the $+x$ direction over the feedback cavity, and the transmitted signal was recollected *via* an outcoupling grating. The incoupling and outcoupling gratings were designed with a pitch $p = 560$ nm to couple photons around the surface normal to SPPs through diffraction by g_1 and with a duty cycle $d = 1/2$ to avoid a g_2 stop gap. The feedback cavity ($p = 280$ nm, d varied) was centered between the incoupling and outcoupling gratings with ~15 μm separation in the x direction between each grating. Each grating had a width in the y direction of 10 μm and a length in the x direction (feedback direction) given by the maximum integer multiple of the pitch that yielded a length below 10 μm. The sample was covered with a thin layer of PMMA and was mounted on the microscope, similar to the reflectivity measurements. To launch SPPs propagating only along the x direction, the incoupling grating was illuminated with a broadband halogen lamp from all angles along k_x with $k_y / k_0 \approx 0$ by projecting a custom excitation mask onto the back focal plane of the microscope objective. The light diffracted from the outcoupling grating was collected with the objective and imaged onto the entrance slit of the imaging spectrograph. The transmitted signal, a slice of the real-space image along the centers of the three gratings, was spectrally dispersed to obtain x-resolved transmission spectra. A detailed description of the optical setup and the data processing is available in Section S3 of the Supporting Information.

Design of Plasmonic Lasers. Each plasmonic laser consisted of a feedback cavity and two outscattering gratings. The duty cycle of the g_2-feedback (g_1-feedback) cavity was $d = 3/4$ (1/2) to maximize the feedback rate, and the pitch $p_c = 435$ nm (201 nm) was chosen to spectrally overlap the higher-energy g_2 (g_1) stop-gap edge with the gain envelope of the NPLs. (While the lowest lasing thresholds were found for lasing at ~1.95 eV, a slight detuning from this configuration was chosen to minimize excitation-fluence-dependent blue-shifting of the lasing peak.) The outscattering gratings were designed to diffract SPPs to photons that leave close the surface close to normal through g_1 diffraction by selecting a pitch of p_c ($2p_c$) when g_2-feedback (g_1-feedback) cavities were studied. The

reflective stop gap was minimized for the outscattering gratings by selecting a duty cycle of 1/2. The feedback cavity (outscattering gratings) had a width in the y direction of 10 μm (20 μm) and a length in the x direction given by the maximum integer multiple of the pitch that yielded a length below 10 μm (5 μm). The feedback cavity and outscattering gratings were separated in the x direction by ~2.5 μm.

Lasing Experiments. The plasmonic samples covered with NPLs were mounted on a piezo positioning system inside a closed-cycle helium cryostat and cooled to ~4 K (see schematic of the optical setup in Figure S4b in the Supporting Information). The NPLs were optically excited at 480 nm (2.583 eV) using an excitation laser pulsed at 100 Hz. The excitation laser was prepared such that the sample was illuminated through an objective (NA of 0.7) with a flat-top illumination profile (equal pump intensity at every position inside the pumped area). The pumped area was also restricted to a rectangular region using custom excitation masks. Only an area that included the feedback cavity or the feedback cavity, the outscattering gratings, and the area in between were excited, as indicated in the main text. The emission from the sample was collected with the same objective and sent through a 488-nm long-pass dichroic beam splitter, a 590-nm long-pass filter, and a relay-lens system into an imaging spectrograph. The resulting images were recorded with an air-cooled electron-multiplying charge-coupled device (EMCCD) camera. For momentum-resolved emission spectra, a Fourier lens was added in the collection path to project the Fourier plane of the emission onto the entrance slit, and the signal passing the slit (a slice through k-space around $k_y / k_0 = 0$) was spectrally dispersed and recorded with the EMCCD camera. For real-space images of the emission at the lasing wavelength, tunable short-pass and long-pass filters were placed in the collection path and were adjusted to act as a narrow band-pass filter around the lasing wavelength. The slit, the Fourier lens, and the dispersion grating were removed, and the sample plane was imaged onto the camera. The Fourier lens could be added to this configuration to obtain k-space images of the emission at the lasing wavelength.

ASSOCIATED CONTENT

Supporting Information. The Supporting Information is available free of charge on the ACS Publications website at https://pubs.acs.org.

Detailed descriptions of the sample fabrication (Section S1), modeling (Section S2), and optical measurements (Section S3).

AUTHOR INFORMATION

Corresponding Author

*Email: dnorris@ethz.ch.

ORCID

Raphael Brechbühler: 0000-0001-7498-9729

Sander J. W. Vonk: 0000-0002-4650-9473

Nolan Lassaline: 0000-0002-5854-3900

Robert C. Keitel: 0000-0002-9412-8034

Marianne Aellen: 0000-0003-1548-0433

Ario Cocina: 0000-0003-1560-5849

Aurelio A. Rossinelli: 0000-0001-6930-4190

Freddy T. Rabouw: 0000-0002-4775-0859

David J. Norris: 0000-0002-3765-0678

Note

The authors declare no competing financial interest.

REFERENCES

(1)   Barnes, W. L.; Dereux, A.; Ebbesen, T. W. Surface Plasmon Subwavelength Optics. *Nature* **2003**, *424*, 824–830.

(2)   Maier, S. A. *Plasmonics: Fundamentals and Applications*; Springer: New York, NY, 2007.

(3)   Gramotnev, D. K.; Bozhevolnyi, S. I. Plasmonics beyond the Diffraction Limit. *Nat. Photonics* **2010**, *4*, 83–91.

(4)   Nie, S.; Emory, S. R. Probing Single Molecules and Single Nanoparticles by Surface-Enhanced Raman Scattering. *Science* **1997**, *275*, 1102–1106.

(5)   Cai, W.; Vasudev, A. P.; Brongersma, M. L. Electrically Controlled Nonlinear Generation of Light with Plasmonics. *Science* **2011**, *333*, 1720–1723.

(6)   Kauranen, M.; Zayats, A. V. Nonlinear Plasmonics. *Nat. Photonics* **2012**, *6*, 737–748.

(7)   Salamin, Y.; Baeuerle, B.; Heni, W.; Abrecht, F. C.; Josten, A.; Fedoryshyn, Y.; Haffner, C.; Bonjour, R.; Watanabe, T.; Burla, M.; Elder, D. L.; Dalton, L. R.; Leuthold, J. Microwave Plasmonic Mixer in a Transparent Fibre–Wireless Link. *Nat. Photonics* **2018**, *12*, 749–753.

(8)   Haffner, C.; Joerg, A.; Doderer, M.; Mayor, F.; Chelladurai, D.; Fedoryshyn, Y.; Roman, C. I.; Mazur, M.; Burla, M.; Lezec, H. J.; Aksyuk, V. A.; Leuthold, J. Nano–Opto-Electro-Mechanical Switches Operated at CMOS-Level Voltages. *Science* **2019**, *366*, 860–864.

(9)   Ayata, M.; Fedoryshyn, Y.; Heni, W.; Baeuerle, B.; Josten, A.; Zahner, M.; Koch, U.; Salamin, Y.; Hoessbacher, C.; Haffner, C.; Elder, D. L.; Dalton, L. R.; Leuthold, J. High-Speed Plasmonic Modulator in a Single Metal Layer. *Science* **2017**, *358*, 630–632.

(10)   Tian, J.; Yu, S.; Yan, W.; Qiu, M. Broadband High-Efficiency Surface-Plasmon-Polariton Coupler with Silicon-Metal Interface. *Appl. Phys. Lett.* **2009**, *95*, 7–10.

(11)   Tetienne, J.-P.; Bousseksou, A.; Costantini, D.; De Wilde, Y.; Colombelli, R. Design of an Integrated Coupler for the Electrical Generation of Surface Plasmon Polaritons. *Opt. Express* **2011**, *19*, 18155.

(12)   Costantini, D.; Greusard, L.; Bousseksou, A.; Rungsawang, R.; Zhang, T. P.; Callard, S.; Decobert, J.; Lelarge, F.; Duan, G. H.; De Wilde, Y.; Colombelli, R. *In Situ* Generation of Surface Plasmon Polaritons Using a Near-Infrared Laser Diode. *Nano Lett.* **2012**, *12*, 4693–4697.

(13)   Sudarkin, A. N.; Demkovich, P. A. Excitation of Surface Electromagnetic Waves on the Boundary of a Metal with an Amplifying Medium. *Sov. Phys. Tech. Phys.* **1989**, *34*, 764–766.

(14)   Bergman, D. J.; Stockman, M. I. Surface Plasmon Amplification by Stimulated Emission of Radiation: Quantum Generation of Coherent Surface Plasmons in Nanosystems. *Phys. Rev. Lett.* **2003**, *90*, 027402.

(15)   Oulton, R. F.; Sorger, V. J.; Zentgraf, T.; Ma, R.-M.; Gladden, C.; Dai, L.; Bartal, G.; Zhang, X. Plasmon Lasers at Deep Subwavelength Scale. *Nature* **2009**, *461*, 629–632.

(16) Berini, P.; De Leon, I. Surface Plasmon–Polariton Amplifiers and Lasers. *Nat. Photonics* **2012**, *6*, 16–24.

(17) Kress, S. J. P.; Cui, J.; Rohner, P.; Kim, D. K.; Antolinez, F. V.; Zaininger, K.-A.; Jayanti, S. V.; Richner, P.; McPeak, K. M.; Poulikakos, D.; Norris, D. J. A Customizable Class of Colloidal-Quantum-Dot Spasers and Plasmonic Amplifiers. *Sci. Adv.* **2017**, *3*, e1700688.

(18) Zhu, W.; Xu, T.; Wang, H.; Zhang, C.; Deotare, P. B.; Agrawal, A.; Lezec, H. J. Surface Plasmon Polariton Laser Based on a Metallic Trench Fabry-Perot Resonator. *Sci. Adv.* **2017**, *3*, e1700909.

(19) Aellen, M.; Rossinelli, A. A.; Keitel, R. C.; Brechbühler, R.; Antolinez, F. V.; Cui, J.; Norris, D. J. Reconsidering the Design of Planar Plasmonic Lasers: Gain, Gap Layers, and Mode Competition. 2021, arXiv:2101.05881. arXiv.org e-Print archive. https://arxiv.org/abs/2101.05881 (accessed Jan 15, 2021).

(20) Lakhani, A. M.; Kim, M.; Lau, E. K.; Wu, M. C. Plasmonic Crystal Defect Nanolaser. *Opt. Express* **2011**, *19*, 18237.

(21) Hill, M. T.; Marell, M.; Leong, E. S. P.; Smalbrugge, B.; Zhu, Y.; Sun, M.; van Veldhoven, P. J.; Geluk, E. J.; Karouta, F.; Oei, Y.-S.; Nötzel, R.; Ning, C.-Z.; Smit, M. K. Lasing in Metal-Insulator-Metal Sub-Wavelength Plasmonic Waveguides. *Opt. Express* **2009**, *17*, 11107.

(22) Marell, M. J. H.; Smalbrugge, B.; Geluk, E. J.; van Veldhoven, P. J.; Barcones, B.; Koopmans, B.; Nötzel, R.; Smit, M. K.; Hill, M. T. Plasmonic Distributed Feedback Lasers at Telecommunications Wavelengths. *Opt. Express* **2011**, *19*, 15109.

(23) Lu, Y.-J.; Kim, J.; Chen, H.-Y.; Wu, C.; Dabidian, N.; Sanders, C. E.; Wang, C.-Y.; Lu, M.-Y.; Li, B.-H.; Qiu, X.; Chang, W.-H.; Chen, L.-J.; Shvets, G.; Shih, C.-K.; Gwo, S. Plasmonic Nanolaser Using Epitaxially Grown Silver Film. *Science* **2012**, *337*, 450–453.

(24) Chen, H. Z.; Hu, J. Q.; Wang, S.; Li, B.; Wang, X. Y.; Wang, Y. L.; Dai, L.; Ma, R. M. Imaging the Dark Emission of Spasers. *Sci. Adv.* **2017**, *3*, e1601962.

(25) Van Beijnum, F.; Van Veldhoven, P. J.; Geluk, E. J.; De Dood, M. J. A.; 'T Hooft, G. W.; Van Exter, M. P. Surface Plasmon Lasing Observed in Metal Hole Arrays. *Phys. Rev. Lett.* **2013**, *110*, 206802.

(26) Yang, A.; Li, Z.; Knudson, M. P.; Hryn, A. J.; Wang, W.; Aydin, K.; Odom, T. W. Unidirectional Lasing from Template-Stripped Two-Dimensional Plasmonic Crystals. *ACS Nano* **2015**, *9*, 11582–11588.

(27) Tenner, V. T.; de Dood, M. J. A.; van Exter, M. P. Measurement of the Phase and Intensity Profile of Surface Plasmon Laser Emission. *ACS Photonics* **2016**, *3*, 942–946.

(28) Lei, Z.; Chen, X.; Wang, X.; Guo, L. J.; Yang, T. Surface-Emitting Surface Plasmon Polariton Laser in a Second-Order Distributed Feedback Defect Cavity. *ACS Photonics* **2019**, *6*, 612–619.

(29)   Karami Keshmarzi, E.; Tait, R. N.; Berini, P. Single-Mode Surface Plasmon Distributed
        Feedback Lasers. *Nanoscale* **2018**, *10*, 5914–5922.

(30)   Lassaline, N.; Brechbühler, R.; Vonk, S. J. W.; Ridderbeek, K.; Spieser, M.; Bisig, S.; le
        Feber, B.; Rabouw, F. T.; Norris, D. J. Optical Fourier Surfaces. *Nature* **2020**, *582*, 506–510.

(31)   Nagpal, P.; Lindquist, N. C.; Oh, S.-H.; Norris, D. J. Ultrasmooth Patterned Metals for
        Plasmonics and Metamaterials. *Science* **2009**, *325*, 594–597.

(32)   Dionne, J. A.; Verhagen, E.; Polman, A.; Atwater, H. A. Are Negative Index Materials
        Achievable with Surface Plasmon Waveguides? A Case Study of Three Plasmonic
        Geometries. *Opt. Express* **2008**, *16*, 19001.

(33)   Kurvits, J. A.; Jiang, M.; Zia, R. Comparative Analysis of Imaging Configurations and
        Objectives for Fourier Microscopy. *J. Opt. Soc. Am. A* **2015**, *32*, 2082–2092.

(34)   Winkler, J. M.; Rabouw, F. T.; Rossinelli, A. A.; Jayanti, S. V.; McPeak, K. M.; Kim, D. K.;
        Le Feber, B.; Prins, F.; Norris, D. J. Room-Temperature Strong Coupling of CdSe
        Nanoplatelets and Plasmonic Hole Arrays. *Nano Lett.* **2019**, *19*, 108–115.

(35)   Barnes, W. L.; Preist, T. W.; Kitson, S. C.; Sambles, J. R. Physical Origin of Photonic Energy
        Gaps in the Propagation of Surface Plasmons on Gratings. *Phys. Rev. B* **1996**, *54*, 6227–6244.

(36)   Kogelnik, H.; Shank, C. V. Coupled-Wave Theory of Distributed Feedback Lasers. *J. Appl.
        Phys.* **1972**, *43*, 2327–2335.

(37)   van Exter, M. P.; Tenner, V. T.; van Beijnum, F.; de Dood, M. J. A.; van Veldhoven, P. J.;
        Geluk, E. J.; 't Hooft, G. W. Surface Plasmon Dispersion in Metal Hole Array Lasers. *Opt.
        Express* **2013**, *21*, 27422.

(38)   Henry, C. H.; Kazarinov, R. F.; Logan, R. A.; Yen, R. Observation of Destructive Interference
        in the Radiation Loss of Second-Order Distributed Feedback Lasers. *IEEE J. Quantum
        Electron.* **1985**, *21*, 151–154.

(39)   Kazarinov, R.; Henry, C. Second-Order Distributed Feedback Lasers with Mode Selection
        Provided by First-Order Radiation Losses. *IEEE J. Quantum Electron.* **1985**, *21*, 144–150.

(40)   Giannattasio, A.; Hooper, I. R.; Barnes, W. L. Dependence on Surface Profile in Grating-
        Assisted Coupling of Light to Surface Plasmon-Polaritons. *Opt. Commun.* **2006**, *261*, 291–
        295.

(41)   Rossinelli, A. A.; Rojo, H.; Mule, A. S.; Aellen, M.; Cocina, A.; De Leo, E.; Schäublin, R.;
        Norris, D. J. Compositional Grading for Efficient and Narrowband Emission in CdSe-Based
        Core/Shell Nanoplatelets. *Chem. Mater.* **2019**, *31*, 9567–9578.

(42)   Tomar, R.; Kulkarni, A.; Chen, K.; Singh, S.; Van Thourhout, D.; Hodgkiss, J. M.; Siebbeles,
        L. D. A.; Hens, Z.; Geiregat, P. Charge Carrier Cooling Bottleneck Opens Up Nonexcitonic
        Gain Mechanisms in Colloidal CdSe Quantum Wells. *J. Phys. Chem. C* **2019**, *123*, 9640–
        9650.

(43) Grim, J. Q.; Christodoulou, S.; Di Stasio, F.; Krahne, R.; Cingolani, R.; Manna, L.; Moreels, I. Continuous-Wave Biexciton Lasing at Room Temperature Using Solution-Processed Quantum Wells. *Nat. Nanotechnol.* **2014**, *9*, 891–895.

(44) Guo, K.; Koenderink, A. F. Spatial Intensity Distribution in Plasmonic Particle Array Lasers. *Phys. Rev. Appl.* **2019**, *11*, 024025.

(45) McPeak, K. M.; Jayanti, S. V.; Kress, S. J. P.; Meyer, S.; Iotti, S.; Rossinelli, A.; Norris, D. J. Plasmonic Films Can Easily Be Better: Rules and Recipes. *ACS Photonics* **2015**, *2*, 326–333.
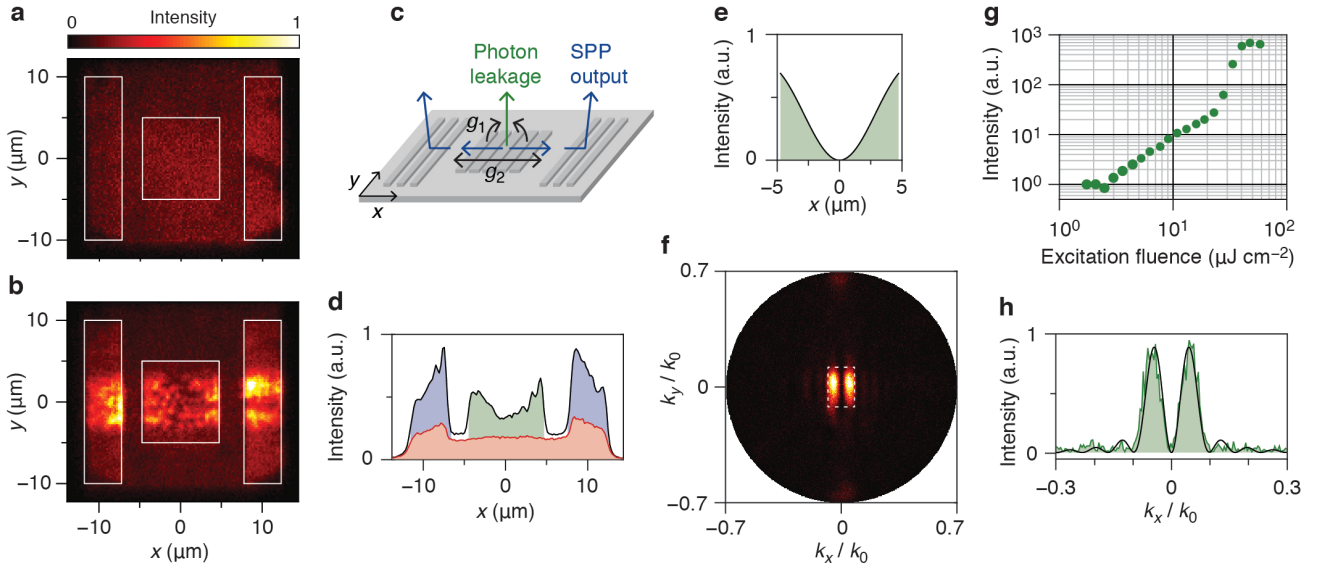
Figures
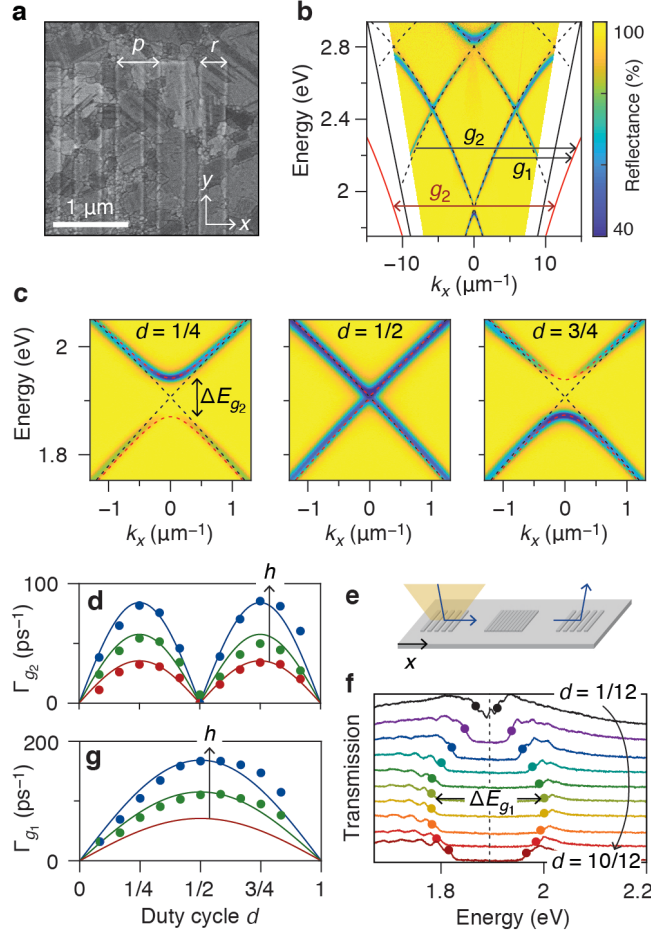
Figure 1. Characterization of plasmonic distributed-feedback cavities without a gain material. (a) Scanning-electron micrograph of a template-stripped Ag grating with $p = 560$ nm, $d = 2/3$, and $h = 13$ nm. (b) Momentum-resolved reflectivity spectrum of the grating from (a) after deposition of ~50 nm of PMMA. Red lines depict the calculated SPP dispersion; black solid lines indicate the light lines; black dashed lines show the calculated grating dispersion without mode coupling. (c) Close-up on momentum-resolved reflectivity spectra at the g_2-feedback condition for cavities with $p = 560$ nm, $h = 13$ nm, and $d = 1/4$, 1/2, and 3/4, respectively. Calculated grating dispersion with (red dashed lines) and without (black dashed lines) mode coupling. (d) Feedback rate at the g_2-feedback condition extracted from reflectivity measurements (filled circles) for cavities with $h = 8$ nm (red), 13 nm (green), and 19 nm (blue). Solid lines are fits to an analytical expression (see main text). (e) Schematic of the experimental SPP-transmission setup to probe the g_1 stop gap. (f) SPP-transmission spectra for cavities with $p = 280$ nm, $h = 19$ nm, and $d = 1/12$ to 10/12 in steps of 1/12 from top to bottom. The calculated stop-gap center is depicted as a vertical dashed line. The stop-gap edges are marked with filled circles and were determined as half-maximum points of the transmission signal at the corresponding side of the stop gap. (g) Feedback rate at the g_1-feedback condition. Color code identical to (d). The collected transmission signal from the shallowest gratings (red line) was too weak to extract stop-gap widths. The data in (c)–(d), (f), and (g) were obtained for gratings covered with ~50 nm of PMMA, as in (b).
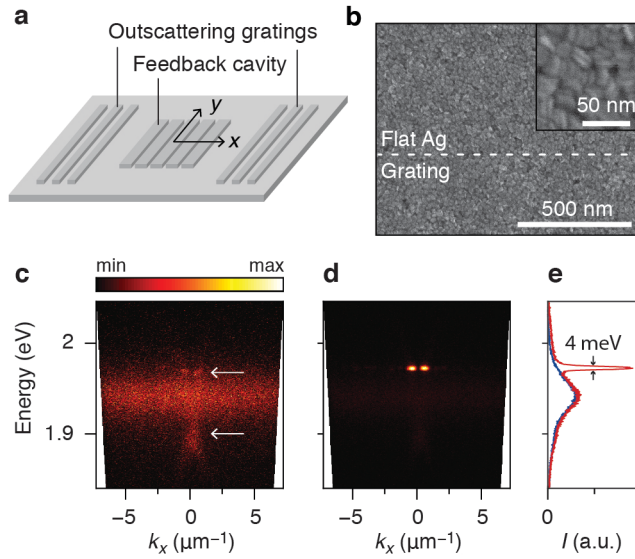
Figure 2. Plasmonic lasing from cavities with g_2 feedback. (a) Schematic of the arrangement of the lasing (feedback) cavity and outscattering gratings (gain layer not shown). (b) Scanning-electron micrograph of a Ag surface with a deposited layer of colloidal nanoplatelets as gain material. The white dashed line indicates the edge of the grating. Inset shows magnified view. (c–e) Plasmonic lasing upon optical pumping of a cavity with $p = 435$ nm, $d = 3/4$, and $h = 11$ nm. The area surrounding the feedback cavity remained unpumped. (c) Below-threshold and (d) above-threshold momentum-resolved emission maps at excitation fluences of 23 and 52 μJ cm^{-2}, respectively. Arrows indicate the energies of the higher- and lower-energy g_2 stop-gap edges. Plasmonic lasing is observed at the higher-energy stop-gap edge in (d). (e) Emission spectra integrated over all collected k_x values from (c) and (d), depicted as blue and red lines, respectively. The intensity of the broad spontaneous-emission feature remains constant above threshold, indicating efficient funneling of optical excitations from the NPLs on the feedback cavity into the lasing mode.

Figure 3. Characterization of the lasing-mode profile for a cavity with g_2 feedback upon optical pumping of the feedback cavity, the outscatterers, and the area in between. (a) Below-threshold and (b) above-threshold real-space photoluminescence images upon optical pumping with 19 and 39 μJ cm^{-2}, respectively. The emission spectrum is filtered with a spectrally narrow band-pass filter to collect signal only at the lasing energy. White boxes indicate the positions of the feedback cavity (square box in center) and outscattering gratings (rectangular boxes on left and right). The intensities are scaled with the excitation fluences used in the respective experiments to keep the spontaneous-emission background at a comparable color level. (c) Schematic of the two output pathways of the lasing signal in (b): direct photon leakage *via* diffraction by g_1 on the feedback cavity (green) and propagating SPPs collected as photons *via* the outscattering gratings (blue). (d) Crosscuts through data of (b) averaged over $|y| < 5$ μm (black line) and 5 μm $< |y| < 10$ μm (red line). Green (blue) area is an estimate for lasing output *via* direct photon leakage (propagating SPPs); red area indicates the estimated spontaneous-emission background. (e) Above-threshold real-space mode profile diffracted to the far field on the feedback cavity calculated with coupled-wave theory. (f) Experimental lasing leakage signal collected in k-space (excitation fluence of 40 μJ cm^{-2}). Only signal from the feedback cavity is collected. (g) Intensity of the lasing leakage signal integrated over the white dashed box from (f) as a function of the excitation fluence. (h) Crosscut through the experimental data of (f) at $k_y / k_0 = 0$ (green) and the calculated k-space pattern (black) corresponding to the real-space profile from (e).

23
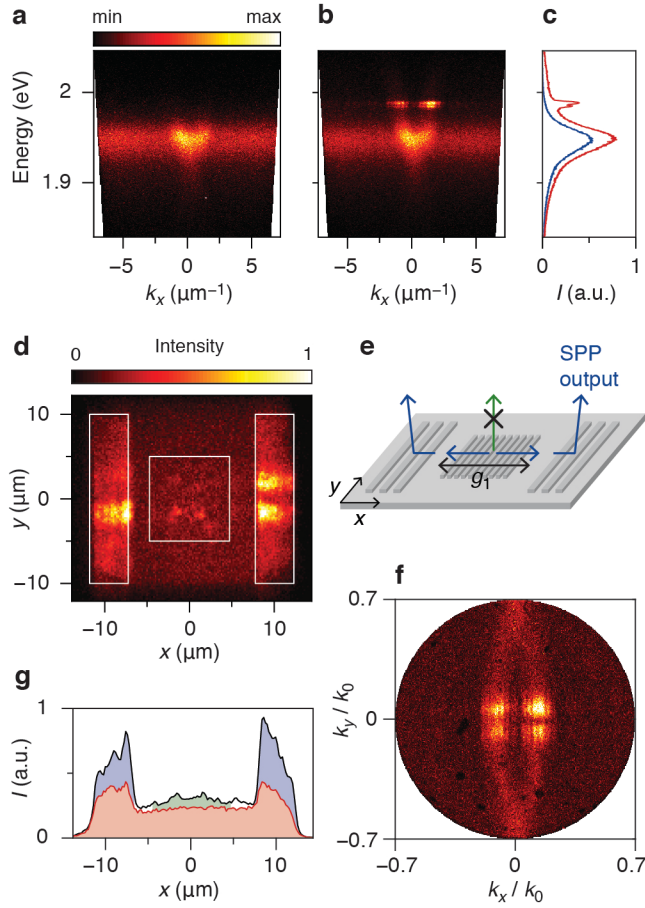
Figure 4. Plasmonic lasing for a "dark" cavity with g_1 feedback upon optical pumping of the feedback cavity, the outscatterers, and the area in between. (a) Below-threshold and (b) above-threshold momentum-resolved emission maps at excitation fluences of 13 and 40 $\mu J\,cm^{-2}$, respectively. Dispersion features stem from the outscattering gratings. (c) Emission spectra integrated over all collected k_x values for (a) and (b), depicted as blue and red lines, respectively. (d) Above-threshold real-space image of the lasing emission (excitation fluence of 40 $\mu J\,cm^{-2}$), spectrally filtered to collect signal only at the lasing wavelength. The feedback cavity (inside the white box in the center) stays dark above the lasing threshold. (e) Schematic of the feedback cavity (center) and the outscattering gratings (left and right). The lasing signal leaves the feedback cavity as SPPs in the $\pm x$ directions and diffracts into photons *via* the outscattering gratings (blue) while diffractive photon leakage on the feedback cavity is prohibited (green). (f) Lasing output from (d) plotted in k-space. The two arcs correspond to SPP–photon coupling on the outscattering gratings and the signal at small k_y is the lasing signal diffracted at the outscattering gratings. (g) Crosscuts through (d) averaged over $|y| < 5$ μm (black line) and 5 $\mu m < |y| < 10$ μm (red line). Blue (green) area is an estimate for lasing output *via* propagating SPPs (photon leakage); red area indicates the estimated spontaneous-emission background.

Table of Contents Graphic